Pressure induced bandgap energy increase in a metal iodate

Akun Liang[1], Lan-Ting Shi[2], Robin Turnbull[1], Francisco Javier Manjón[3], Jordi Ibáñez[4], Catalin Popescu[5], M. Jasmin[6], Jaspreet Singh[7], Kanchana Venkatakrishnan[7], Ganapathy Vaitheeswaran[8], Daniel Errandonea[1, *]

[1]Departamento de Física Aplicada—ICMUV, Universitat de València, MALTA Consolider Team, Edificio de Investigación, c/ Dr. Moliner 50, 46100 Burjassot, Valencia, Spain

[2]Institute of High Energy Physics, Chinese Academy of Sciences (CAS), 100049, Beijing, China.

[3]Instituto de Diseño para la Fabricación y Producción Automatizada, MALTA Consolider Team, Universitat Politècnica de València, Camí de Vera s/n, 46022 València, Spain

[4]Geosciences Barcelona (GEO3BCN), Malta Consolider Team, CSIC, 08028, Barcelona, Spain

[5]CELLS-ALBA Synchrotron Light Facility, Cerdanyola, 08290, Barcelona, Spain

[6]TKM College of Arts and Science, 691005, Kerala, India

[7]Department of Physics, Indian Institute of Technology Hyderabad, Kandi-502285, Sangareddy, Telangana, India

[8]School of Physics, University of Hyderabad, Prof. C. R. Rao Road, Gachibowli, Hyderabad, 500046, Telangana, India

Corresponding author: daniel.errandonea@uv.es

Abstract

A wide bandgap is one of the essential requirements for metal iodates to be used as non-linear optical materials. Usually, the bandgap of these materials decreases under the application of pressure. Herein, we introduce the first case in which the bandgap energy of a hydrated metal iodate, namely $Ca(IO_3)_2 \cdot H_2O$, has been successfully increased, from 4.52 eV to 4.92 eV, by applying external pressure without showing sign of saturation upon increasing pressure. The pressure-induced nonlinear bandgap opening correlates with the pressure-induced shortening of the average I-O bond distance, as obtained from X-ray diffraction measurements. In addition, two pressure-induced isostructural phase transitions are observed in the pressure regions of 6.6-8.0 GPa and 13.0-15.5 GPa. These two isostructural phase transitions cause a nonlinear pressure-induced evolution of the bandgap energy and crystal lattice parameter, as well as the occurrence of several extra peaks and peak splitting in Raman spectra.

I. INTRODUCTION

Due to the existence of the stereochemically-active lone electron pairs and the non-zero dipole moment in the iodate group, $[IO_3]^-$, iodates of metals (known as metal iodates) typically crystallize with non-centrosymmetric crystal structures and exhibit a large second-harmonic generation response [1]. By carefully designing and manipulating the orientation of the polar units, it is possible to synthesize metal iodates with an ultrahigh second-harmonic generation response. For example, the second-harmonic generation responses of $BaNbO(IO_3)_5$ and $LiMg(IO_3)_3$ are respectively about 14 and 24 times larger than that of KH_2PO_4, the most widely used second-order non-linear optical material [2,3].

In order to be successfully implemented as non-linear optical materials, a compound needs to have: (i) A large second-harmonic generation response; (ii) a moderate birefringence; (iii) a wide transparency region; (iv) a high laser damage threshold; and (v) a good chemical stability. The large second-harmonic generation response is needed for a highly efficient laser conversion and the moderate birefringence for an optimized phase matching. The wide transparency region (large bandgap) is needed to allow the converted laser light to exit the non-linear optical crystal without being absorbed by promoting electrons from the valence band to the conduction band. Finally, the good chemical stability is needed for practical applications and the high laser damage threshold (also related to a large bandgap) is needed to avoid damage of the non-linear optical material by laser irradiation. In summary, a wide bandgap energy is essential for the implementation of metal iodates as non-linear optical materials.

As our previous studies have shown, there are two important factors to consider in the design of wide bandgap metal iodates [4,5]: (i) Avoiding the use of partially filled transition metals, because the 3*d* state of the partially filled metal will contribute to either the valence band maxima or the conduction band minima, and thus narrow the bandgap energy [5]. Some partially filled 3*d* states with appropriate coordination can also exhibit photo-absorption related to internal *d*-*d* transitions [6]. (ii) Minimizing the I-O bond distance, because there is an inversely proportional relationship between the bandgap energy and the I-O bond distance in non-transition metal or closed-shelled transition metal iodates [4]. This means that shortening the I-O bond distance increases the bandgap energy of metal iodates.

Pressure is an efficient and clean external parameter for manipulating the interatomic distances in materials and, therefore, also for tuning the bandgap energy. Indeed, we have found that the bandgap energies of $Zn(IO_3)_2$ [4], $Mg(IO_3)_2$ [4], $Fe(IO_3)_3$ [5], and $Co(IO_3)_2$ [6], all decrease under compression. Moreover, we have demonstrated a relation between the decrease of the bandgap with pressure in those compounds and the pressure dependence of their I-O bond distances. Since the crystal structures of each of these four metal iodates share the similar feature of layers containing IO_3 pyramids, and since all the IO_3 units are aligned in a parallel manner, in all four of these iodates the average bond distance between I and the 3 nearest neighbor O atoms expands under compression due to the pressure-induced approach of the 3 next-nearest O atoms from the neighboring IO_3 layer. Therefore, in the case of the four previously studied metal iodates, pressure shortens the large I-O next-nearest neighbor bond distance whilst enlarging the shorter I-O nearest neighbor distance. This enlargement of the short I-O bond distances causes the narrowing of the bandgap energy with increasing pressure in the four aforementioned metal iodates.

The above result suggests that if pressure is applied on non-transition or closed-shell transition metal iodates, in which not all IO_3 units are aligned along the same direction, the average I-O bond distance could be shortened by external pressure and the bandgap energy could be opened as pressure increases. Consequently, we chose $Ca(IO_3)_2 \cdot H_2O$ to perform this high-pressure study of a non-transition metal iodate. The hydrated calcium iodate crystallizes in a monoclinic structure at ambient conditions (space group: $P2_1/c$, No. 14, see **Fig. 1**) [7]. The alkaline-earth metal (calcium) is bonded with eight oxygen atoms forming a CaO_8 polyhedron, while iodine is bonded with three oxygen atoms forming a triangular pyramid with short I-O bond distances ranging from 1.7 to 1.9 Å. The CaO_8 polyhedron and IO_3 pyramid are bridged by sharing one oxygen atom between them. Along the *b*-axis, there is an alternating arrangement of CaO_8 and IO_3 layers. Within the IO_3 layers, all the IO_3 units are oriented in different directions. It is this atomic arrangement which ultimately leads to the unexpected pressure-induced opening of the bandgap of hydrated calcium iodate, which supports the model we previously developed to explain the bandgap of metal iodates [4–6].

In this work, we report a pressure-induced nonlinear bandgap opening, from 4.52 eV at ambient pressure to 4.92 eV at 18.7 GPa, in hydrated calcium iodate, making it one of the widest bandgap metal iodates reported in the literature [4]. The bandgap

behavior under compression is correlated with the pressure dependence of the I-O bond distance as determined from high-pressure powder X-ray diffraction measurements. These measurements, complemented with high-pressure Raman scattering experiments, have allowed us to identify two pressure-induced isostructural phase transitions that cause the nonlinear behavior of the bandgap under compression.

II. METHODS

A. Sample synthesis

The single diffusion gel technique is found to be a simple strain free method for synthesizing single crystals with high purity, optical perfection, and wide morphology at room temperature. The gel having density 1.03 g/cm^3 was prepared by dissolving sodium meta silicate $Na_2SiO_3 \cdot 9H_2O$ in double distilled water. Potassium iodate having molarity 0.5M is incorporated into the gel medium. The above prepared gel medium was acidified by adding glacial acetic acid to get the pH value 4.2. This acidified gel solution is transferred through the sides of the test tubes which is 20 cm in length and 2.5 cm in diameter to avoid the air bubbles inside the gel medium. These test tubes were kept undisturbed for three days to set the gel solution. Over this set gel 10 ml of 0.25 M calcium chloride solution was added. The test tubes were sealed to avoid the contamination. This setup was kept undisturbed for the growth process to be completed. Hexagonal shaped white transparent good quality single crystals were obtained within one week. The fine powder sample was obtained by grinding a single crystal sample under a liquid medium (to obtain a smaller and more homogenous particle size) in a pestle and mortar. To avoid contamination, we used the same liquid mixture used as pressure-transmitting medium in high-pressure experiments.

B. Optical absorption experiments at high pressure

A membrane-type of diamond anvil cell was used to generate the high-pressure environments, and the culets of the diamond used in the diamond anvil cell were 400 μm in diameter. Stainless-steel was used as the gasket material. The gasket was pre-indented to a thickness of 40 μm and a 200-μm hole, drilled in the center of the indentation area, served as the sample chamber. A single crystal sample, with a

thickness of 10 μm, was selected and placed into the sample chamber together with a ruby sphere. A photograph of the loading at the lowest pressure can be found in the insert image of **Fig. 2a** in the main manuscript. The ruby fluorescence method was employed for the pressure calibration [8]. A mixture of methanol, ethanol, and water in a ratio of 16:3:1 was chosen as the pressure-transmitting medium, which can provide the hydrostatic conditions up to around 10 GPa [9].

The high-pressure optical absorption experiment was conducted in a bespoke optical system, which contains a mercury lamp (the range of the lamp is down to 220 nm), fused silica lenses, reflecting optics objectives, and a visible near-Infrared spectrometer (Ocean Optics Maya2000 Pro). The sample-in and sample-out method was used to collect the absorption spectra, in which the intensity of the light transmitted through the sample [$I(\omega)$] was normalized against the intensity transmitted through an empty area in the pressure-transmitting medium [$I_0(\omega)$].

C. Powder X-ray diffraction experiments at high pressure

High-pressure angle-dispersive powder X-ray diffraction was performed at the BL04-MSPD beamline in ALBA-CELLS synchrotron [10]. A membrane-type diamond anvil cell was used to generate the high-pressure environment and the culets of the diamond were 500 μm. The preparation of the gasket used here is the same as that in the high-pressure optical absorption experiment. A mixture of methanol, ethanol, and water in a ratio of 16:3:1 was used as pressure-transmitting medium, a copper grain was loaded in the sample chamber with the powder sample and the equation of state of copper was used as the pressure calibration [11]. The wavelength of the monochromatic X-ray beam was 0.4246 Å, and the size of the beam spot is 20 × 20 μm (full width at half maximum). The sample-to-detector distance was calibrated by the high purity LaB_6 powder, and the diffraction image was recorded with a Rayonix SX165 charge-coupled device detector. The diffraction image was integrated to the two-dimensional X-ray diffraction pattern by using the DIOPTAS program [12]. The Rietveld refinement of the powder pattern was performed in the FullProf suites [13].

D. Raman scattering experiments at high pressure

These experiments have been performed using a single crystal sample. A membrane-type of diamond anvil cell with the diamond culets of 500 μm was used to

generate the high-pressure environments. Here, the preparation of the gasket is the same as that in the high-pressure optical absorption experiment. A mixture of methanol, ethanol and water in a ratio of 16:3:1 was used as pressure-transmitting medium, and the ruby fluorescence method was used as the pressure calibration [8]. A He/Ne laser with a wavelength of 632.8 nm of 20 mW power was used as the light source and the microspectrometer was a HORIBA Jobin Yvon LabRAM HR UV model. A thermoelectrically cooled multichannel charge-coupled device detector with a resolution better than 2 cm^{-1} was used to collect the signal. The setup was calibrated by helium plasma lines for the spectra in the ruby fluorescence region and silicon Raman-active modes for the Raman spectra region.

E. Calculation details

The *ab initio* total-energy of $Ca(IO_3)_2 \cdot H_2O$ was calculated based on density function theory [14] as implanted in the Vienna Ab initio Simulation Package (VASP) [15], where with the pseudopotential method according to the projector-augmented wave scheme [16] to treat the full nodal character of the all electron charge density in the core region. The basis set of the plane waves was extended with to a reasonable energy cut off 500 eV to achieve an accurate description of the electronic properties. The exchange-correlation interaction was considered in the generalized-gradient approximation, which is parametrized with the Perdew-Burke-Ernzerhof function [17]. For optimized configurations, the forces on the atoms were less than 0.0001 $eV \cdot Å^{-1}$, and it is worthy of note that all the simulations were performed at zero temperature (T = 0). In order to determine the interaction between different atoms, we calculated the crystal orbital overlap population by the Lobster code [18].

III. RESULTS AND DISCUSSION

A. Bandgap behavior under pressure

Fig. 2a shows the absorption edge of $Ca(IO_3)_2 \cdot H_2O$. The measured absorption edge is shaper and has a weaker absorption tail than in our previous experiments in other iodates [4–6] because in the present study a single crystal was used for the measurements whereas in the previous experiments we used platelets obtained from

compressed powder. The absorption edge of $Ca(IO_3)_2 \cdot H_2O$ shows a blue shift under pressure (**Fig. 2a**), indicating a pressure-induced bandgap opening (**Fig. 2b**). Our theoretical calculations of the electronic band structure (**Fig. S1** in Supplemental Information (**SI**) [19]) show that $Ca(IO_3)_2 \cdot H_2O$ is an indirect bandgap material at ambient pressure. Therefore, the Tauc plot for indirect bandgap materials was used (**Fig. S2** in **SI** [19]) to obtain the bandgap energy at each pressure [20]. The high-energy part of the $(\alpha h\nu)^{1/2}$ vs $h\nu$ has been fitted by a linear function and extrapolated to zero. α, h, and ν are the absorption coefficient, Planck's constant, and the photon frequency, respectively. As plotted in **Fig. 2b**, the bandgap of $Ca(IO_3)_2 \cdot H_2O$ is 4.52 eV at ambient pressure and increases under compression to 4.70 eV at 7.9 GPa (Phase I). Upon further compression the bandgap energy shows an almost pressure independent behavior up to 15.3 GPa (Phase II). Finally, in Phase III, the bandgap energy increases dramatically from 4.79 eV at 16.3 GPa up to 4.92 eV at 18.7 GPa. The bandgap of diamond in the diamond anvil cell precluded acquisition of data at higher pressures [21]; however, based on the results shown in **Fig. 2b** and the crystal structure evolution, which we will show later, we expect the bandgap of $Ca(IO_3)_2 \cdot H_2O$ to increase continuously and become larger than 5 eV above 20 GPa.

B. Crystal structure evolution under compression

Powder X-ray diffraction patterns of $Ca(IO_3)_2 \cdot H_2O$ collected at high pressure are shown in **Fig. 3a** up to 19.7 GPa. No extra reflections, reflection splitting, or disappearing reflections are observed over the whole pressure range. In fact, all patterns can be indexed with the original monoclinic $P2_1/c$ structure [7] as shown by the Rietveld refinements [13] of the representative powder X-ray diffraction patterns collected at the lowest pressure (0.4 GPa) and highest pressure (19.7 GPa) in **Fig. 3b**. The pressure-induced changes of the X-ray diffraction patterns are totally reversible upon sample decompression. The pattern collected after decompression (see **Fig. 3a**) and the Rietveld refinement (see **Fig. 3b**) support this conclusion. The quality factors of the Rietveld refinement are R_p=1.35%, R_{wp}=2.12% (0.4 GPa), R_p=12.4%, R_{wp}=12.2% (19.7 GPa) and R_p=1.15%, R_{wp}=1.71% (ambient pressure released), respectively. All peaks shift to higher angles due to the contraction of the three lattice parameters (**Fig. 3c**) of the crystal structure under compression. At pressures higher than 12 GPa, the intensity of the peaks decreases dramatically, and the peaks become broadened, which

is attributed to the gradual solidification of the pressure-transmitting medium used in the high-pressure experiment [9].

A monotonic decrease in the lattice parameters with small changes of slope as pressure increases are observed (**Fig. 3c**). The changes of slope correlate with strong changes in the slope of the monoclinic angle at similar pressures regions (**Fig. 3d**). In particular, the drastic slope changes occur in the pressure region of 7.0-8.0 GPa and 13.0-15.0 GPa. This can be interpreted because of the occurrence of two pressure-induced isostructural phase transitions. Similar pressure-induced isostructural transitions have been observed in other metal iodates, for instance, $Fe(IO_3)_3$ [22], $Zn(IO_3)_2$ [23], and $Co(IO_3)_2$ [24]. More evidence of the occurrence of the isostructural phase transitions can be found in the Raman spectra presented later. Notably, the pressures at which the slope change in the lattice parameters and monoclinic angle agree with those at which changes happen in the bandgap energy. Here, following the name assignment used when describing the optical studies, we name the three phases as Phases I, II, and III.

A second-order Birch-Murnaghan equation of state (wherein the pressure derivative of the bulk modulus, B_0', is fixed equal to 4.0) [25] as incorporated in EoSFit 7c [26] was used to fit the lattice parameters of Phase I (**Fig. S3** in **SI** [19]). The zero-pressure value obtained from the fits for the three axis were: a_0 = 8.532(2) Å, b_0 = 10.069(1) Å, and c_0 = 7.545(1) Å. The bulk moduli of the lattice parameters *a*, *b*, and *c* were 52.8(9) GPa, 33.2(2) GPa, and 26.5(2) GPa, respectively. This means that the most compressible axis is the *c* axis. Notably, the crystal structure of $Ca(IO_3)_2{\cdot}H_2O$ shows a smaller anisotropic behavior than other metals iodates, such as $Zn(IO_3)_2$ [23], $Co(IO_3)_2$ [24], and $Mg(IO_3)_2$ [27]. We ascribe this feature to the different orientations exhibited by the IO_3 pyramids in $Ca(IO_3)_2{\cdot}H_2O$. In the Zn, Co and Mg iodates, the IO_3 units are aligned in the same direction and there is a large gap between the $[IO_3]^-$ layers which is not exhibited in $Ca(IO_3)_2{\cdot}H_2O$.

No apparent volume discontinuity occurs at the mentioned transition pressures in $Ca(IO_3)_2{\cdot}H_2O$, as shown by the unit-cell volume obtained from the Rietveld refinements (**Fig. 3e**). In fact, the combined data for all 3 phases can be described with a single third-order Birch-Murnaghan equation of state with a volume at zero pressure (V_0) of 641.8(5) $Å^3$, a bulk modulus (B_0) of 39.0 (7) GPa and a pressure derivative (B_0') of 4.0(1); i.e. the obtained equation of state is compatible with a second-order equation (B_0' = 4.0). The bulk modulus is larger than those of $Zn(IO_3)_2$ (21.6 GPa) [23],

$Co(IO_3)_2$ (29.8 GPa) [24], $Mg(IO_3)_2$ (22.2 GPa) [27], α-$LiIO_3$ (34 GPa) [28], and KIO_3 (24.3 GPa) [29], but smaller than that of $Fe(IO_3)_3$ (55 GPa) [28].

In order to determine the pressure dependence of the I-O distances, and to study their relation with the observed changes in the bandgap, we have to consider that the iodine atoms are located at two different Wyckoff positions in the crystal structure of $Ca(IO_3)_2{\cdot}H_2O$. For both iodine atoms, there are two types of I-O distances at ambient conditions (**Fig. 4a**): i) Three short I-O distances in the range of 1.7 to 1.9 Å that constitute the short I-O bonds that exist at room pressure and lead to threefold coordination of I atoms. ii) Three long I-O distances in the range of 2.8 to 3.2 Å that do not form bonds at room pressure, but they do at high pressure and leading to a six-fold coordination of I atoms. Our previous studies on metal iodates showed that formation of the three long I-O bonds are a consequence of the presence of a lone electron pair in the iodine atom and that pressure helps to transform the lone electron pair into three additional bonds [5,22].

In $Ca(IO_3)_2{\cdot}H_2O$, the average long I-O bond distance shortens under compression from the ambient pressure up to around 13.5 GPa and remains insensitive to pressure between 13.5 GPa and 18 GPa (**Fig. 4d**). On the other hand, the average short I-O bond distance shows a less sensitive behavior of pressure from the ambient pressure up to around 7.5 GPa (in this pressure range changes are comparable to error bars) and a slight increase in the pressure region of 7.5-13.5 GPa, which is followed by a considerable decrease between 13.5 GPa and 18 GPa (**Fig. 4c**). The slope changes observed in the average long/short I-O bond distance occur at the same pressures as the slope changes in the bandgap energy (**Fig. 2b**) and the slope changes in the lattice parameters and monoclinic angle (**Figs. 3c and 3d**).

In order to correlate changes in the bandgap and in the I-O bond distances, we have calculated the electronic density of states (DOS), the projected density of states (PDOS, **Fig. S4** in **SI** [19]), and the crystal orbital overlap population (**Fig. S5** in **SI** [19]) between the iodine atom (I2) and the six nearest oxygen atoms. In this way, we have been able to depict the molecular orbital diagram of $Ca(IO_3)_2{\cdot}H_2O$ at ambient pressure (**Fig. S6** in **SI** [19]) and its detail near the Fermi level **(Fig. 4b**). Since the observed phase transitions are isostructural, it is not expected that pressure would induce a substantial change in the topology of the band structure as was found in $Fe(IO_3)_3$ [5]. Therefore, the molecular orbital diagram can be used to explain not only the bandgap at ambient pressure but also over the complete pressure range covered by our study, as

seen in $Mg(IO_3)_2$ and $Zn(IO_3)_2$ [4]. The molecular orbital diagram near the Fermi level reflects that the bandgap energy is largely determined by the *p-p* orbital interaction between iodine and oxygen atoms (the full discussion of the complete molecular orbital diagram of the interaction between iodine and oxygen could be found in **SI** [19]). In particular, the valence band maximum in the electronic band structure is dominated by O-2*p* non-bonding orbitals and the conduction band minima is dominated by anti-bonding O-2*p* and I-5*p* orbitals. This profile of the band structure is consistent with the common feature of the band structure for non-transition metal iodates [4,5]. In summary, the bandgap of $Ca(IO_3)_2 \cdot H_2O$ is primarily determined by the energy difference between the O-2*p* non-bonding state and the anti-bonding state of the *p-p* interaction between iodine and oxygen atoms.

Since the pressure-induced opening or closing of the bandgap is mainly related to the different shift rates of the conduction band minima with respect to the valence band maximum, the pressure-dependence of the bandgap is, to a first approximation, dominated by the behavior of the average distance of short I-O bonds under compression, since the interaction in the short I-O bonds is much stronger than that in the long I-O bonds (**Fig. S5** in **SI** [19]). The contribution of the change of the average distance of long I-O bonds under compression will, therefore, be of a second order. However, if the short bonds are little affected by pressure, then a large change in length of the long I-O bonds will affect the behavior of the bandgap energy. Notice that, if the I-O bond distance shortens under compression, the hybridization of the *p-p* interaction between iodine and oxygen is enhanced, increasing the separation between bonding and anti-bonding states, and thereby opening the bandgap. In contrast, the expansion of the I-O bond distance will cause a decrease of the bandgap energy. In Phase I of $Ca(IO_3)_2 \cdot H_2O$, the changes of the average short I-O distances are much smaller than in other iodates; indeed, changes are comparable to error bars (**Fig. 4c**); i.e. they can be considered to remain nearly constant under pressure. Thus, the large decrease observed in the average long I-O distance (**Fig. 4d**) will cause the observed increase of the bandgap energy (**Fig. 2b**). In Phase II, the slight increase of the short I-O bond distance narrows the bandgap energy, compensated by the effect from the shortening of the long I-O bonds. In summary, the bandgap shows an independent behavior in this pressure region of Phase II (**Fig. 2b**). In contrast, in Phase III, the short I-O bond distances decrease with increasing pressure (**Fig. 4c**) dominating the behavior of the bandgap and causing a very rapid opening of the bandgap energy in this pressure region (**Fig. 2b**).

C. Evidence of the pressure-induced isostructural phase transition from Raman experiments

Finally, it should be stressed that Raman spectroscopy is an efficient tool for the detection of the local rearrangement of atoms and for the characterization of pressure-induced phase transitions [30,31]. The Raman spectra of $Ca(IO_3)_2 \cdot H_2O$ at selected pressures are plotted in **Fig. 5a**. A waterfall plot of all the Raman spectra collected under high pressure could be found in **Fig. S7** in **SI** [19]. The Raman spectra collected at ambient pressure shares the same features as in $Zn(IO_3)_2$ [23], $Co(IO_3)_2$ [24], and $Mg(IO_3)_2$ [27] and can be divided into three regions. The high-frequency region is located from 700 to 800 cm^{-1} and Raman modes in this region have been assigned to the symmetric and asymmetric stretching of $[IO_3]^-$ units [24,27]. The most intense peak is usually observed in this region [22–24,27]. The middle-frequency region is located between 300 to 400 cm^{-1} and Raman modes in this region are attributed to the symmetric and asymmetric bending of $[IO_3]^-$ units [24,27]. Finally, the low-frequency region is located below 300 cm^{-1} and the Raman modes of this region can be related to the translational and rotational motions of the iodate molecule as a rigid unit.

In **Fig. 5a,** on increasing pressure, there is one Raman peak appearing at the lowest frequency in the high-frequency region if we compare the Raman spectra collected at ambient pressure and 3.3 GPa (it can be also observed in **Fig. S8** in **SI** [19]). These changes cannot be caused by a phase transition since no transition is detected by either of the other two diagnostic techniques used in this work. Actually, this vibrational mode exists at ambient pressure but it overlaps with the next Raman mode in the same region. The pressure dependence of this mode has been shown in red triangle in **Fig. S8** in SI [19], Therefore, the appearance of the new mode is related to the splitting of degenerate modes. Notice that, according to group theory, the studied compound has 72 Raman-active modes, however only 22 are observed at ambient-pressure because of mode degeneracy. The splitting of modes is a typical phenomenon in compounds with anisotropic compressibility such as $Ca(IO_3)_2 \cdot H_2O$. Other changes, like the growing in intensity of some Raman modes in the middle- and low-frequency region, observed in this pressure range could be related to acquiring Raman spectra from parts of the sample with different orientations. Furthermore, the disappearance of some Raman peaks in the low- or high-frequency region is caused by merging with the neighboring peaks.

More intense extra Raman peaks appear at 6.6 GPa at both the high- and middle-

frequency regions (see upward arrows in **Fig. 5a**). Moreover, two Raman modes at around 750 cm^{-1} at ambient pressure, show a totally different pressure coefficient before and after 6.6 GPa (**Fig. 5b** and **Fig. S8** in **SI** [19]). All these changes confirm the first isostructural phase transition as we found in optical-absorption and X-ray diffraction experiments. Notice that the changes in the Raman spectrum are not caused by a decrease of the crystal symmetry, (since the phase transitions are isostructural,) but by local changes in the atomic coordination due to the anisotropic compressibility of the studied material. The changes in the high- and middle-frequency region are related to the pressure-induced oxygen coordination increase of iodine. In particular, an increase of coordination usually leads to a decrease of the phonon gap between bending and stretching modes, as it happens for instance on the transition from scheelite to fergusonite [32]. Therefore, the extra modes of the high-frequency region with Raman shifts below 700 cm^{-1} are consistent with the increase of iodine coordination above 6 GPa. The emerging modes can be interpreted in this way: As the long I-O bond distances continuously shorten under compression and the stereo-activity of the iodine lone electron pairs decreases, the iodine starts to gradually bond with the oxygen in the neighboring $[IO_3]^-$ units to form additional IO_6 units. Therefore, extra internal (both bending and stretching) modes of the IO_6 units appear in the middle- and high-frequency regions, respectively.

Additionally, some Raman mode splitting appears at 14.1 GPa (inset in **Fig. 5a**). This fact coincides with the occurrence of the second pressure-induced isostructural phase transition. The reasons for changes in the Raman spectra are related to changes in the coordination of Ca and I and not to a changes in the crystal symmetry. According to the X-ray diffraction experiments, the crystal symmetry does not change over the entire studied pressure range. The lowest energy Raman modes in the high-frequency region show a softening behavior in Phases I and II, which can be observed in **Fig. 5b** and **Fig. S8** [19]. This is a result of the enlargement of the short I-O bonds under compression since the frequency of the Raman modes correlates with the average I-O bond distance as observed in $Zn(IO_3)_2$ [23]. The pressure-induced changes in the Raman spectra are mostly reversible upon decompression (**Fig. S7** [19]), however, upon compression a shoulder at the low energy side of the high-frequency region becomes more apparent that it initially was at ambient pressure. This mode existed at ambient pressure but overlapped with the neighboring Raman modes, and it becomes more apparent on decompression due to a slight hysteresis in the sample.

IV. CONCLUSIONS

The bandgap energy of $Ca(IO_3)_2 \cdot H_2O$ has been increased from 4.52 eV at ambient pressure up to 4.92 eV at 18.7 GPa, thus making this material becomes one of the most transparent metal iodates reported in the literature. The successful engineering of the bandgap energy is attributed to the pressure-induced shortening of the average long or short I-O bond distance. We explain this phenomenon by building a molecular orbital diagram for $Ca(IO_3)_2 \cdot H_2O$ based on density-functional theory calculations. This model shows that the bandgap energy of $Ca(IO_3)_2 \cdot H_2O$ is dominated by the non-bonding O-2*p* states and anti-bonding states of the *p*-*p* interaction between I and O atoms. The bandgap energy and the I-O bond distance therefore exhibit an inverse relationship. The bandgap also shows a non-linear behavior under compression up to 18 GPa due to the existence of two pressure-induced isostructural phase transitions located at 6.6-8.0 GPa and 13.0-15.5 GPa, respectively, as evidenced by the non-linear behavior of the lattice parameters and by the appearance of extra peaks in the Raman spectra. All changes of the structural, vibrational, and optical properties were found to be reversible upon release of pressure.

ACKNOWLEDGMENTS

This study was supported by project MALTA Consolider Team network (RED2018-102612-T), financed by MINECO/AEI/10.13039/501100003329, I+D+i project PID2019-106383GB-41/42 financed by MCIN/AEI/10.13039/501100011033; as well as by projects PROMETEO CIPROM/2021/075 (GREENMAT) and MFA/2022/007 financed by Generalitat Valenciana. A.L. and D.E. thank the Generalitat Valenciana for the Ph.D. Fellowship No. GRISOLIAP/2019/025. R.T. and D.E. thank the Generalitat Valenciana for the postdoctoral Fellowship No. CIAPOS/2021/20. The authors also thank ALBA synchrotron light source for funded experiment under proposal number AV-2021095390 at the MSPD-BL04 beamline.

References

[1] H. Y. Chang, S. H. Kim, M. O. Kang, and P. S. Halasyamani, Polar or Nonpolar? A^+ Cation Polarity Control in $A_2Ti(IO_3)_6$ (A = Li, Na, K, Rb, Cs, Tl), J. Am. Chem. Soc. **131**, 6865 (2009).

[2] C. F. Sun, C. L. Hu, X. Xu, J. B. Ling, T. Hu, F. Kong, X. F. Long, and J. G. Mao, $BaNbO(IO_3)_5$: A New Polar Material with a Very Large SHG Response, J. Am. Chem. Soc. **131**, 9486 (2009).

[3] J. Chen, C. L. Hu, F. F. Mao, X. H. Zhang, B. P. Yang, and J. G. Mao, $LiMg(IO_3)_3$: An Excellent SHG Material Designed by Single-Site Aliovalent Substitution, Chem. Sci. **10**, 10870 (2019).

[4] A. Liang, R. Turnbull, P. Rodríguez-hernandez, A. Muñoz, M. Jasmin, L. Shi, and D. Errandonea, General Relationship between the Band-Gap Energy and Iodine-Oxygen Bond Distance in Metal Iodates, Phys. Rev. Mater. **6**, 044603 (2022).

[5] A. Liang, P. Rodríguez-Hernandez, A. Munoz, S. Raman, A. Segura, and D. Errandonea, Pressure-Dependent Modifications in the Optical and Electronic Properties of $Fe(IO_3)_3$: The Role of Fe 3*d* and I 5*p* Lone-Pair Electrons, Inorg. Chem. Front. **8**, 4780 (2021).

[6] A. Liang, F. Rodríguez, Rodríguez-Hernandez， P, A. Muñoz, R. Turnbull, and D. Errandonea, High-Pressure Tuning of *d–d* Crystal-Field Electronic Transitions and Electronic Band Gap in $Co(IO_3)_2$, Phys. Rev. B **105**, 115204 (2022).

[7] G. E. Ericksen, M. E. Mrose, and J. W. Marinenko, Mineralogical Studies of the Nitrate Deposits of Chile: VI. Brüggenite,$Ca(IO_3)_2 \cdot H_2O$, a New Saline Mineral, J. Res. U.S. Geol. Surv. **2**, 471 (1974).

[8] H. K. Mao, J. Xu, and P. M. Bell, Calibration of the Ruby Pressure Gauge to 800 Kbar under Quasi-Hydrostatic Conditions, J. Geophys. Res. **91**, 4673 (1986).

[9] S. Klotz, J. C. Chervin, P. Munsch, and G. Le Marchand, Hydrostatic Limits of 11 Pressure Transmitting Media, J. Phys. D. Appl. Phys. **42**, 075413 (2009).

[10] F. Fauth, I. Peral, C. Popescu, and M. Knapp, The New Material Science Powder Diffraction Beamline at ALBA Synchrotron, Powder Diffr. **28**, 360 (2013).

[11] A. Dewaele, P. Loubeyre, and M. Mezouar, Equations of State of Six Metals above 94 GPa, Phys. Rev. B **70**, 094112 (2004).

[12] C. Prescher and V. B. Prakapenka, DIOPTAS: A Program for Reduction of Two-Dimensional X-Ray Diffraction Data and Data Exploration, High Press. Res. **35**, 223 (2015).

[13] J. Rodríguez-Carvajal, Recent Advances in Magnetic Structure Determination by Neutron Powder Diffraction, Phys. B Phys. Condens. Matter **192**, 55 (1993).

[14] P. Hohenberg and W. Kohn, Inhomogeneous Electron Gas, Phys. Rev. **136**, B864 (1964).

[15] G. Kresse and J. Furthmüller, Efficient Iterative Schemes for Ab Initio Total-Energy Calculations Using a Plane-Wave Basis Set, Phys. Rev. B **54**, 11169 (1996).

[16] P. E. Blöchl, Projector Augmented-Wave Method, Phys. Rev. B **50**, 17953 (1994).

[17] J. P. Perdew, K. Burke, and M. Ernzerhof, Generalized Gradient Approximation Made Simple, Phys. Rev. Lett. **77**, 3865 (1996).

[18] S. Maintz, V. L. Deringer, A. L. Tchougréeff, and R. Dronskowski, LOBSTER: A Tool to Extract Chemical Bonding from Plane-Wave Based DFT, J. Comput. Chem. **37**, 1030 (2016).

[19] See Supplemental Information at “URL to Be Added by Editor” for the Description of Molecular Orbital Diagram, Calculated Electronic Band Structure, DOS, Crystal Orbital Overlap Population, Experimental Raman

Spectra at All Pressure and Pressure Dependence of Raman Modes.
[20] J. Tauc, Optical Properties and Electronic Structure of Amorphous Ge and Si, Mater. Res. Bull. **3**, 37 (1968).
[21] R. S. Balmer, J. R. Brandon, S. L. Clewes, H. K. Dhillon, J. M. Dodson, I. Friel, P. N. Inglis, T. D. Madgwick, M. L. Markham, T. P. Mollart, N. Perkins, G. A. Scarsbrook, D. J. Twitchen, A. J. Whitehead, J. J. Wilman, and S. M. Woollard, Chemical Vapour Deposition Synthetic Diamond: Materials, Technology and Applications, J. Phys. Condens. Matter **21**, 364221 (2009).
[22] A. Liang, S. Rahman, P. Rodriguez-Hernandez, A. Muñoz, F. J. Manjón, G. Nenert, and D. Errandonea, High-Pressure Raman Study of $Fe(IO_3)_3$: Soft-Mode Behavior Driven by Coordination Changes of Iodine Atoms, J. Phys. Chem. C **124**, 21329 (2020).
[23] A. Liang, C. Popescu, F. J. Manjon, A. Muñoz, Z. Hebboul, and D. Errandonea, Structural and Vibrational Study of $Zn(IO_3)_2$ Combining High-Pressure Experiments and Density-Functional Theory, Phys. Rev. B **103**, 054102 (2021).
[24] A. Liang, C. Popescu, F. J. Manjon, R. Turnbull, E. Bandiello, P. Rodriguez-Hernandez, A. Muñoz, I. Yousef, Z. Hebboul, and D. Errandonea, Pressure-Driven Symmetry-Preserving Phase Transitions in $Co(IO_3)_2$, J. Phys. Chem. C **125**, 17448 (2021).
[25] F. D. Murnaghan, Finite Deformations of an Elastic Solid, Am. J. Math. **59**, 235 (1937).
[26] R. J. Angel, J. Gonzalez-Platas, and M. Alvaro, EosFit7c and a Fortran Module (Library) for Equation of State Calculations, Zeitschrift Fur Krist. **229**, 405 (2014).
[27] A. Liang, R. Turnbull, C. Popescu, F. J. Manjón, E. Bandiello, A. Muñoz, I. Yousef, Z. Hebboul, and D. Errandonea, Pressure-Induced Phase Transition and Increase of Oxygen-Iodine Coordination in Magnesium Iodate, Phys. Rev. B **105**, 054105 (2022).
[28] A. Liang, S. Rahman, H. Saqib, P. Rodriguez-Hernandez, A. Munoz, G. Nenert, I. Yousef, C. Popescu, and D. Errandonea, First-Order Isostructural Phase Transition Induced by High Pressure in $Fe(IO_3)_3$, J. Phys. Chem. C **124**, 8669 (2020).
[29] L. Bayarjargal, L. Wiehl, A. Friedrich, B. Winkler, E. A. Juarez-Arellano, W. Morgenroth, and E. Haussühl, Phase Transitions in KIO_3, J. Phys. Condens. Matter **24**, 325401 (2012).
[30] R. Turnbull, M. E. Donnelly, M. Wang, M. Peña-Alvarez, C. Ji, P. Dalladay-Simpson, H. K. Mao, E. Gregoryanz, and R. T. Howie, Reactivity of Hydrogen-Helium and Hydrogen-Nitrogen Mixtures at High Pressures, Phys. Rev. Lett. **121**, 195702 (2018).
[31] P. Dalladay-Simpson, R. T. Howie, and E. Gregoryanz, Evidence for a New Phase of Dense Hydrogen above 325 Gigapascals, Nature **529**, 63 (2016).
[32] D. Errandonea, F. J. Manjón, A. Muñoz, P. Rodríguez-Hernández, V. Panchal, S. N. Achary, and A. K. Tyagi, High-Pressure Polymorphs of $TbVO_4$: A Raman and Ab Initio Study, J. Alloys Compd. **577**, 327 (2013).

FIGURES

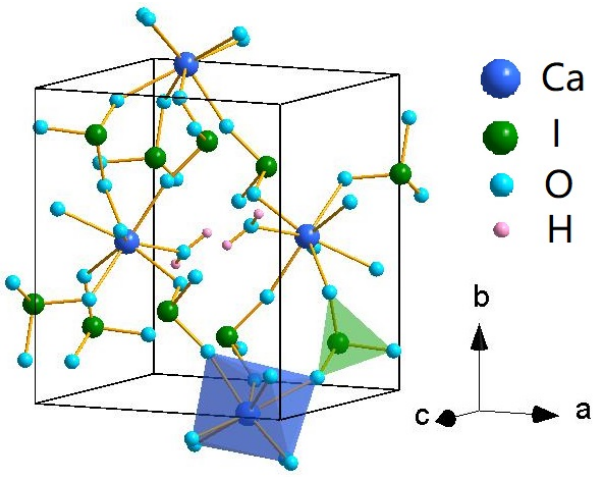

FIG. 1. (Color online) Crystal structure of $Ca(IO_3)_2 \cdot H_2O$ at ambient pressure.

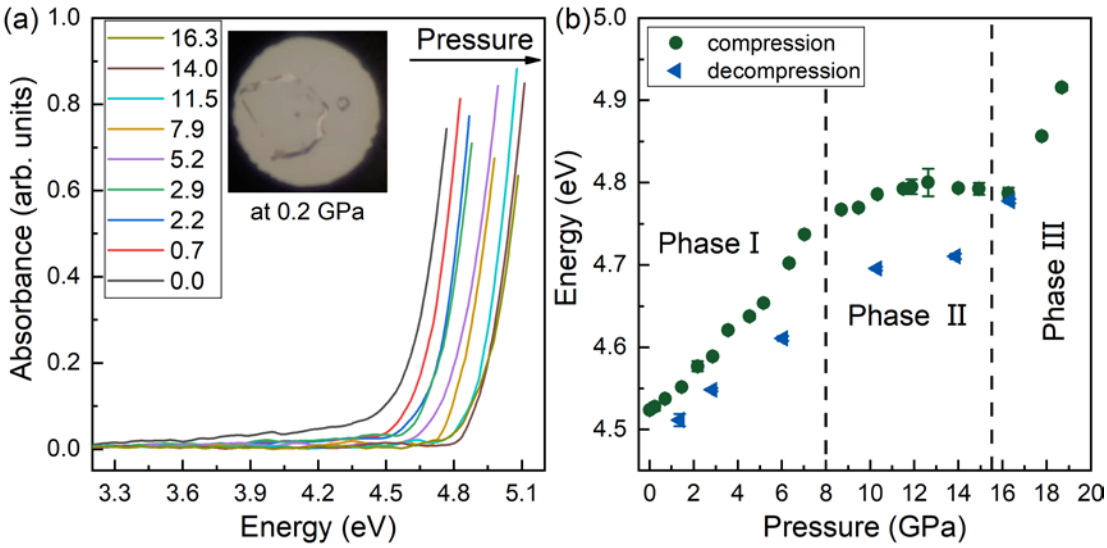

FIG. 2. (Color online) a) Optical-absorption spectra of $Ca(IO_3)_2 \cdot H_2O$ at selected pressures. The sample pressures associated with the spectra are shown in "GPa" in the legend. The inset shows the sample (large crystal) and the ruby chip (small crystal) inside the diamond anvil cell at 0.2 GPa. b) The bandgap energy of $Ca(IO_3)_2 \cdot H_2O$ as a function of pressure, which was derived from the optical absorption spectra in **Fig. 2a** using Tauc plots. The bandgap evolution was divided into three regions based on the gradient of energy *vs.* pressure. The vertical dashed lines indicate the transition pressures.

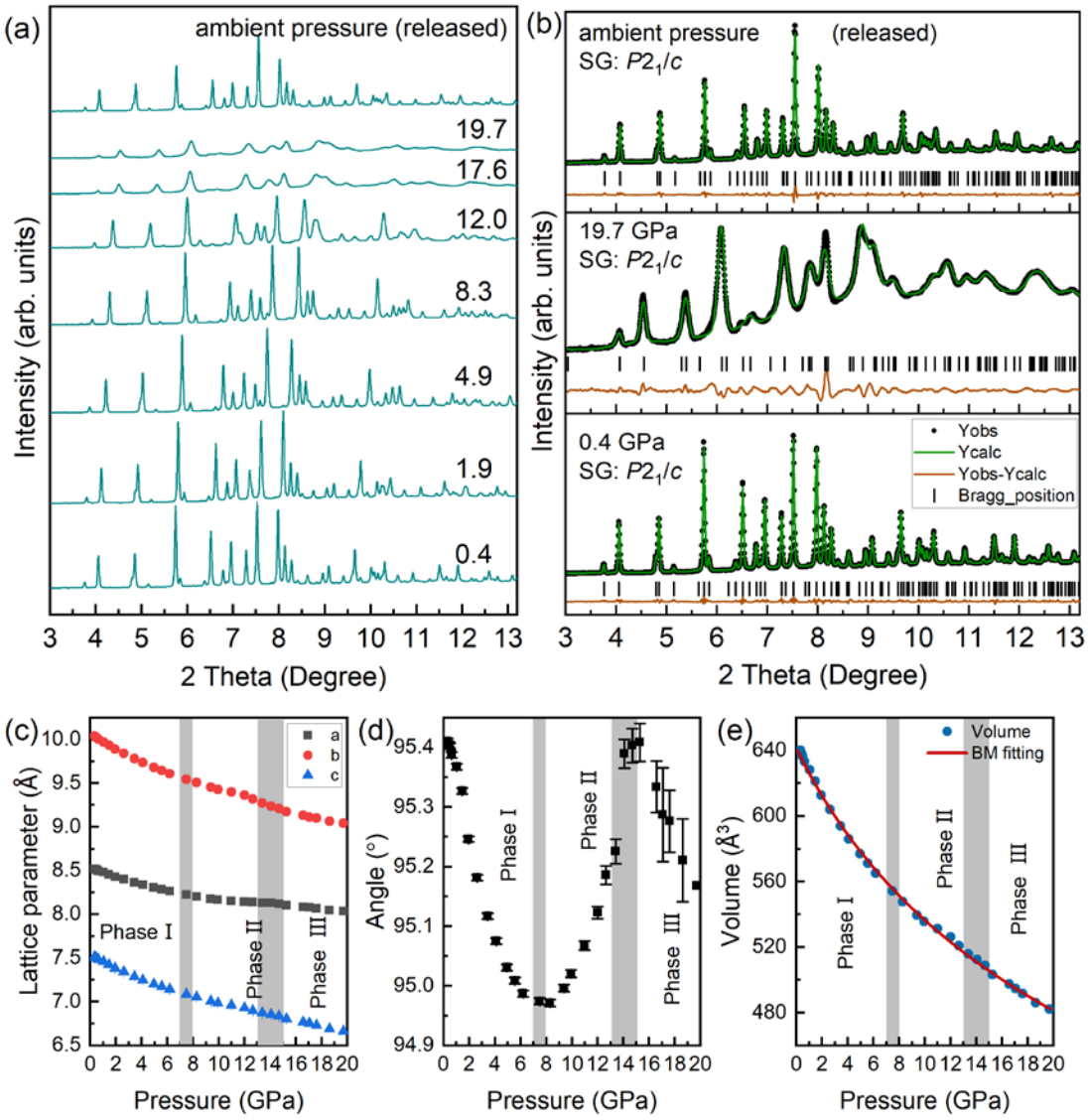

FIG. 3. (Color online) *a*) Powder X-ray diffraction patterns of $Ca(IO_3)_2 \cdot H_2O$ at selected pressures. Pressures are indicated in the right in "GPa". *b*) Rietveld refinements of the X-ray diffraction pattern at 0.4 GPa, 19.7 GPa, and ambient pressure after decompression. Experimental data (Y_{obs}), refined patterns (Y_{calc}), positions of diffraction peaks, and the residuals (Y_{obs}-Y_{calc}) are shown in black dots, green solid line, black ticks, and orange solid lines, respectively. "SG" is the space group of the crystal structure. *c,d,e*) Lattice parameters, monoclinic angle, and unit-cell volume as a function of pressure. Gray regions indicate the pressure ranges in which the isostructural phase transitions occur. The red solid line is the Birch-Murnaghan (BM) fit of the unit-cell volume. In (c) and (e), error bars are smaller than symbols.

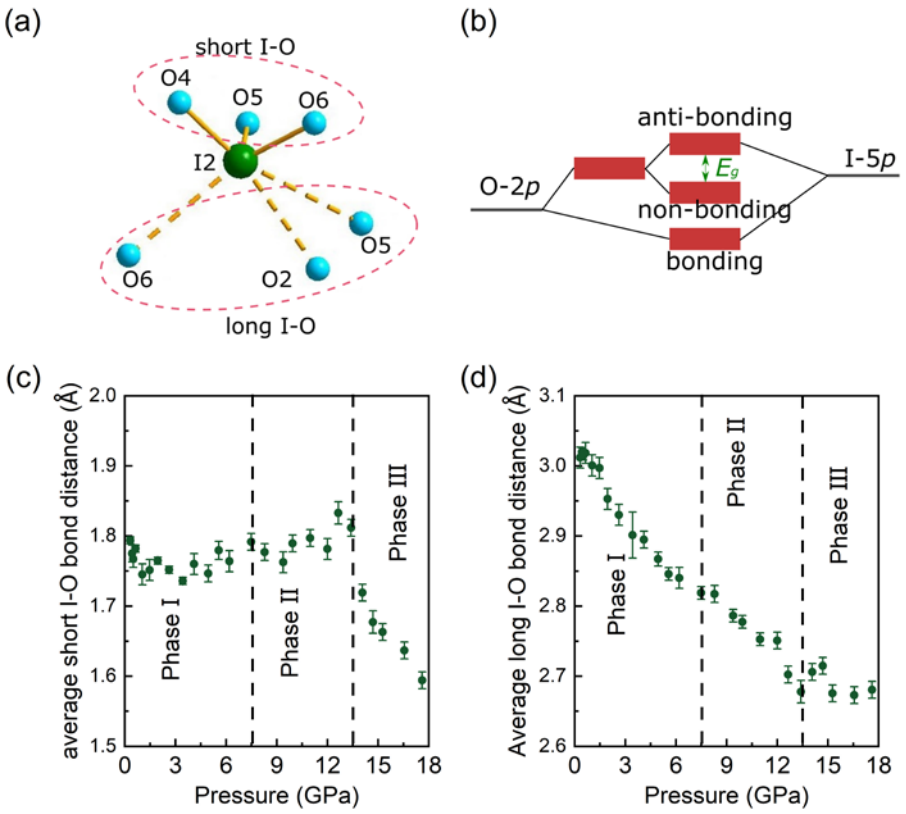

FIG. 4. (Color online) *a*) Representation of the IO_6 polyhedron. The solid bonds are the short I-O bonds that exist at ambient pressure, the dashed bonds are the long I-O distances that become bonds at high pressure. *b*) Molecular orbital diagram near the Fermi level at ambient pressure. *c,d)* Pressure dependence of the average short I-O bond distances and average long I-O bond distances, respectively. All I-O distances are obtained from Rietveld refinements of powder X-ray diffraction patterns. The vertical dashed lines indicate the pressures at which slope changes are observed.

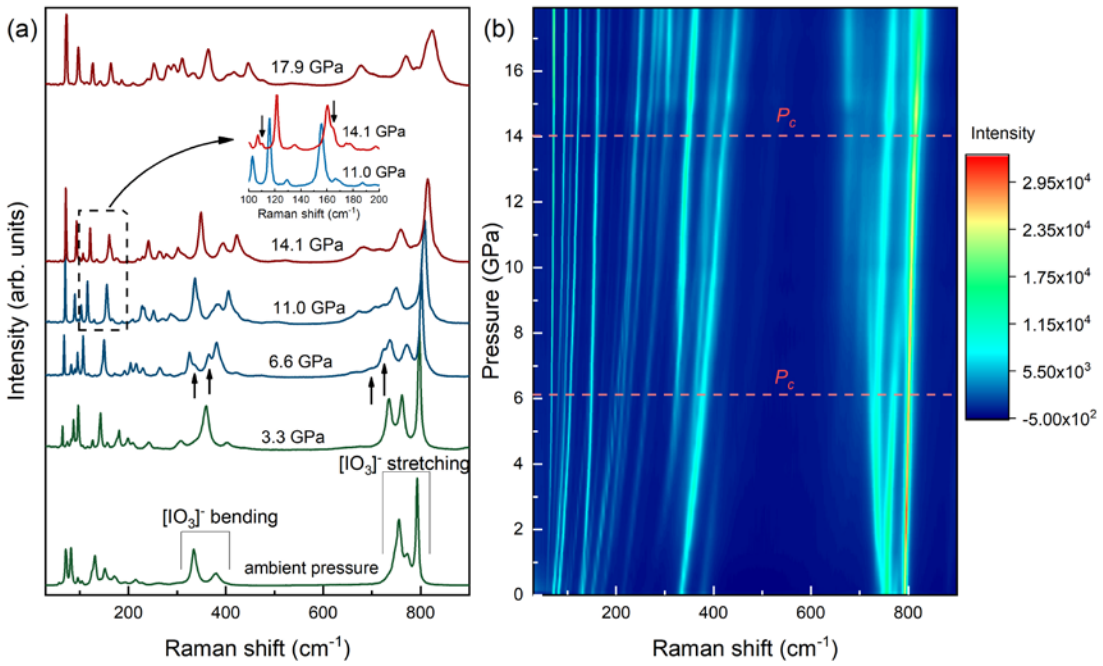

FIG. 5. (Color online) *a*) Raman spectra of $Ca(IO_3)_2 \cdot H_2O$ at selected pressures. The inset figure shows an enlarged representation of the area marked by a dashed square (100-200 cm^{-1}) for the Raman spectra collected at 11.0 GPa and 14.1 GPa. Raman spectra of Phases I, II, and III are shown in green, blue, and red, respectively. The upward and downward arrows indicate the appearance of the additional Raman peaks. *b*) Contour plot of the Raman spectra collected at high pressure. The horizontal dashed lines labeled as "P_c" indicate the transition pressures.